In vivo detection of exercise-induced ultrastructural changes in genetically-altered murine skeletal muscle using polarization-sensitive optical coherence tomography

James J. Pasquesi, Simon C. Schlachter

Department of Electrical and Computer Engineering
Beckman Institute for Science and Technology
University of Illinois at Urbana-Champaign

Marni D. Boppart, Eric Chaney, Stephen J. Kaufman

Department of Cell and Developmental Biology
University of Illinois at Urbana-Champaign

Stephen A. Boppart

Department of Electrical and Computer Engineering, Department of Bioengineering
Beckman Institute for Science and Technology
Colleges of Engineering and Medicine
University of Illinois at Urbana-Champaign
405 N. Mathews Avenue, Urbana, IL 61801
boppart@uiuc.edu

Abstract: Skeletal muscle fibers are a known source of form birefringence in biological tissue. The birefringence present in skeletal muscle is associated with the ultrastructure of individual sarcomeres, specifically the arrangement of A-bands corresponding to the thick myosin filaments. Certain structural proteins that prevent damage and maintain the structural and functional health of the muscle fiber preserve the organization of the A-bands in skeletal muscle. Therefore, the level of birefringence detected can estimate the health of the muscle as well as the damage incurred during exercise. Murine skeletal muscle from both genetically-altered (*mdx*) and normal (wild-type) specimens were imaged *in vivo* with a fiber-based PS-OCT imaging system to quantitatively determine the level of birefringence present in the tissue before and after exercise. The *mdx* muscle lacks dystrophin, a structural protein that is mutated in Duchenne muscular dystrophy in humans. Muscle from these *mdx* mice exhibited a marked decrease in birefringence after exercise, whereas the wild-type muscle was highly birefringent before and after exercise. The quantitative results from this tissue optics study suggest for the first time that there is a distinct relationship between the degree of birefringence detected using PS-OCT and the sarcomeric ultrastructure present within skeletal muscle.

References and links

1. K. P. O'Reilly, M. J. Warhol, R. A. Fielding, W. R. Frontera, C. N. Meredith, and W. J. Evans, "Eccentric exercise-induced muscle damage impairs muscle glycogen repletion," J. Appl. Physiol. **63**, 252 (1987).
2. J. F. Watchko, T. L. O'Day, and E. P. Hoffman, "Functional characteristics of dystrophic skeletal muscle: insights from animal models," J. Appl. Physiol. **93**, 407 (2002).

3.   J. Sherman, A. Vander, and D. Luciano, *Human Physiology: The Mechanisms of Body Function,* 8th ed. New York, NY: the McGraw-Hill Companies, Inc. (2001).
4.   S. De la Porte, S. Morin, and J. Koenig, "Characteristics of skeletal muscle in *mdx* mutant mice," Int. Rev. Cytol **191**, 99 (1999).
5.   A. V. Smolensky, J. Ragozzino, S. H. Gilbert, C. Y. Seow, and L. E. Ford, "Length-dependent filament formation assessed from birefringence increases during activation of porcine tracheal muscle," J. Physiol. **563**, 517 (2005).
6.   M. R. Hee, D. Huang, E. A. Swanson, J. G. Fujimoto, "Polarization-sensitive low-coherence reflectometer for birefringence characterization and ranging", J. Opt. Soc. Am. B **9**, 903-908 (1992).
7.   T. E. Milner and J. F. de Boer, "Review of polarization sensitive optical coherence tomography and Stokes vector determination," J. Biomed. Opt. **7**, 359 (2002).
8.   Y. Chen, L. Otis, D. Piao, and Q. Zhu, "Characterization of dentin, enamel, and carious lesions by a polarization-sensitive optical coherence tomography system," Appl. Opt. **44**, 2041 (2005).
9.   M. C. Pierce, J. Strasswimmer, B. H. Park, B. Cense, and J. F. de Boer, "Birefringence measurements in human skin using polarization-sensitive optical coherence tomography," J. Biomed. Opt. **9**, 287 (2004).
10. W. Drexler, D. Stamper, C. Jesser, X. Li, C. Pitris, K. Saunders, S. Martin, M. B. Lodge, J. G. Fujimoto, and M. E. Brezinski, "Correlation of collagen organization with polarization sensitive imaging of *in vitro* cartilage: implications for osteoarthritis," J. Rheumatol. **28**, 1311 (2001).
11. B. Cense, T. C. Chen, B. H. Park, M. C. Pierce, and J. F. de Boer, "Thickness and birefringence of healthy retinal nerve fiber layer tissue measured with polarization-sensitive coherence tomography," Invest. Ophthalmol. Vis. Sci. **45**, 2606 (2004).
12. S. Guo, J. Zhang, L. Wang, J. S. Nelson, and Z. Chen, "Depth-resolved birefringence and differential optical axis orientation measurements with fiber-based polarization-sensitive optical coherence tomography," Opt. Lett. **29**, 2025 (2004).
13. B. H. Park, M. C. Pierce, B. Cense, and J. F. de Boer, "Jones matrix analysis for a polarization-sensitive optical coherence tomography system using fiber-optic components," Opt. Lett. **29**, 2512 (2004).
14. N. A. Patel, J. Zoeller, D. L. Stamper, J. G. Fujimoto, and M. E. Brezinski, "Monitoring osteoarthritis in the rat model using optical coherence tomography," IEEE Trans. Med. Imaging **24**, 155 (2005).
15. S. Jiao, M. Todorovic, G. Stoica, and L. V. Wang, "Fiber-based polarization-sensitive Mueller matrix optical coherence tomography with continuous source polarization modulation," Appl. Opt. **44**, 5463 (2005).
16. J. F. de Boer, T. E. Milner, and J. S. Nelson, "Determination of the depth-resolved Stokes parameters of light backscattered from turbid media by use of polarization-sensitive optical coherence tomography," Opt. Lett. **24**, 300-302 (1999).
17. C. Hitzenberger, E. Goetzinger, M. Sticker, M. Pircher, and A. F. Fercher, "Measurement and imaging of birefringence and optic axis orientation by phase resolved polarization sensitive optical coherence tomography," Opt. Express **9**, 780-790 (2001), http://www.opticsinfobase.org/abstract.cfm?URI=oe-9-13-780
18. J. de Boer, T. Milner, M. van Gemert, and J. Nelson, "Two-dimensional birefringence imaging in biological tissue by polarization-sensitive optical coherence tomography ," Opt. Lett. **22**, 934-936 (1997).
19. N. Kemp, H. Zaatari, J. Park, H. Rylander III, and T. Milner, "Form-biattenuance in fibrous tissues measured with polarization-sensitive optical coherence tomography (PS-OCT)," Opt. Express **13**, 4611-4628 (2005), http://www.opticsinfobase.org/abstract.cfm?URI=oe-13-12-4611

1. Introduction

Duchenne muscular dystrophy (DMD) is associated with the progressive degeneration of skeletal and cardiac muscle fibers and ultimately leads to death from respiratory or cardiac failure. Acute bouts of intense exercise can induce an inflammatory response as well as ultrastructural changes [1]. DMD is the most frequent form of muscular dystrophy, occurring in approximately 1 out of 3000 males. A recessive gene located on the X chromosome has been identified as the gene responsible for DMD. The gene codes for a protein known as dystrophin, which is a cytoskeletal protein involved in maintaining the structural integrity of muscle cell membranes, and the association of muscle fibers with the surrounding extracellular matrix [2,3]. Due to mutations in this gene, the protein dystrophin is either absent or present in a non-functional form, leaving muscle fibers susceptible to structural damage. Such damage may disrupt A-band organization and alignment, as well as affect the normal association of the muscle fiber with the surrounding basal lamina. Genetically-altered mice, known as *mdx* mice (X–linked muscular dystrophy), have been shown to possess traits similar to DMD (i.e., lacking dystrophin) [4].

The elongated, asymmetrical shape of muscle fibers in general suggests the presence of a fast optical axis. However, the actual source of birefringence in skeletal muscle is highly dependent on biological, physiological, and environmental conditions. A series of light and dark "bands" perpendicular to the long axis of the muscle fiber appear when imaging both skeletal and cardiac muscle fibers through a light microscope. The presence of these bands or striations is due to the arrangement of thick (myosin) and thin (actin) filaments in the myofibrils of the muscle cell. The light and dark bands are referred to as A-bands (anisotropic) and I-bands (isotropic), respectively. The thick (myosin) filaments in the A-bands are considered to be the anisotropic source of form birefringence present in muscle tissue [5]. Therefore, as the presence and organization of thick filaments in muscle type varies, so does the overall birefringence of the tissue.

Polarization-sensitive optical coherence tomography (PS-OCT) is an optical imaging technology that maps depth-resolved changes in the polarization state of light induced by anisotropic tissue properties [6]. By exploiting the interaction between the polarization state of light and biological tissue, additional structural and possibly functional (physiological) information can be extracted [7]. Form birefringence is the main optical property present in biological tissues responsible for altering the polarization state of light. Common sources of form birefringence in biological tissue are muscle, tendons, nerve, bone, cartilage, and teeth. Many of these sources of birefringence have been investigated for potential medical applications [8-15]. However, few PS-OCT investigations have been performed in skeletal muscle, and none of these have investigated the contributions that ultrastructural changes in skeletal muscle have on the tissue optical properties measured by PS-OCT [12, 16].

2. Materials and methods

2.1 Animal studies

Trials were performed *in vivo* on *mdx* (Jackson Labs, Bar Harbor, ME) and wild-type (C57BL6) murine skeletal muscle (gastrocnemius) in compliance with an experimental protocol approved by the Institutional Animal Care and Use Committee at the University of Illinois at Urbana-Champaign. Five-week-old male *mdx* and wild-type mice (n=2/group) were exercised and compared to non-exercised mice from each group (n=2/group). The mice were individually housed, fed daily, and kept on a 12 hour light-dark cycle prior to exercising and imaging. Before *in vivo* PS-OCT was performed, the mice were anaesthetized with xylazine (10mg/kg), ketamine (100mg/kg), and atropine (1mg/kg), and the skin overlaying the gastrocnemius muscle was incised and reflected back, exposing the muscle tissue. A normal (0.9%) saline solution was used prior to imaging to prevent dehydration of the exposed tissue. Controlled exercise of the muscle was used to induce potential ultrastructural changes in myofibers 24 hours prior to imaging. Wild-type and *mdx* mice were run on a rodent treadmill (Exer-6M, Columbus Instruments, Columbus, OH) modified to accommodate a downhill running decline of 20°. Ninety minutes prior to downhill running, wild-type and *mdx* mice were injected with Evans blue fluorescent dye (50 µL/10 g body wt) for later validation studies of muscle injury and damage. The injection of Evans blue fluorescent dye is an established method for visualizing and quantifying muscle injury. In excised specimens, muscle fibers with intact membranes exhibit Evans blue fluorescence localized to regions surrounding the fibers, while the damaged fibers contain Evans blue fluorescence within individual fibers. Wild-type and *mdx* mice were subjected to an exercise protocol that included an initial 2 min warm-up run at a velocity of 10 m/min, followed by a 30 min run at a maximal velocity of 17 m/min. Wild-type mice were able to run for this duration and at this maximal velocity. However, *mdx* mice were only able to complete a run for 25 min at a maximal speed of 15 m/min due to the physical limitations imposed by their genetically-altered muscle.

2.2 Polarization-sensitive OCT system

A schematic of the PS-OCT system used in the experiment is illustrated in Fig. 1. The PS-OCT system was a fiber-based, time-domain system, constructed using a 1300 nm center-wavelength (75 nm bandwidth) SLD source (MenloSystems, Martinsried, Germany). Conventional single-mode optical fiber (SMF-28, Corning, Inc.) was used throughout the system. System parameters included a measured axial resolution of ~10 μm (in free-space), a transverse resolution of ~18 μm, and 5 mW of incident optical power on the specimens. A rapid-scanning optical delay (RSOD) was implemented to perform fast axial scanning at 400 Hz. A polarization controller (P2) was used to align the RSOD polarization state with the state of maximum diffraction efficiency.

A wavelength-independent lithium niobate polarization modulator (EOSpace, Inc.) consisting of a waveguide with single-mode fiber input and output connectors, and a modulator controller, was used to toggle the incident polarization state on the sample between two orthogonal linear states of polarization. The lithium niobate polarization controller was designed to alter (rotate) any input state of polarization to any output polarization state on the Poincaré sphere. The polarization transformation was electro-optically adjusted by varying voltages applied to electrodes surrounding the waveguide. The electric field lines induced between the electrodes alter the optical properties of the waveguide such as birefringence (retardation factor) and fast optical axis orientation. Optical circulators were used to avoid a double-pass through the modulator and promote dual-balance detection.
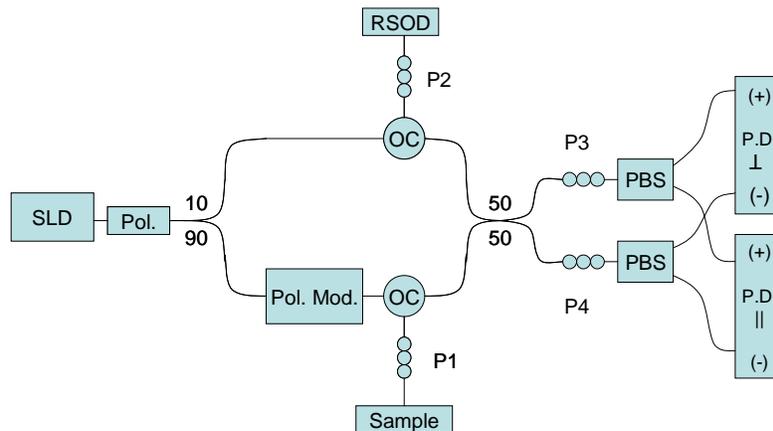

Fig. 1. Schematic of the PS-OCT system. Abbreviations: SLD, super luminescent diode; Pol., linear polarizer; Pol. Mod., polarization modulator; 90/10, 50/50, fiber couplers; RSOD, rapid scanning optical delay; OC, optical circulator; P#, polarization paddles; PBS, polarization beam splitter; P.D., photodetector.

Polarization diversity detection was implemented in order to perform depth-resolved birefringence mapping. The detection scheme also incorporated dual-balance detection in order to improve the system signal-to-noise ratio (SNR). This involved two balanced photodetectors receiving orthogonal polarization states of light from the output fibers of a polarization beam splitter (PBS). The polarization-controlling paddles (P3 and P4) were implemented to balance the reference arm power equally between the two detectors. Additional control signals were used to perform the following tasks: (1) synchronize the toggling of the modulator electrodes with each axial scan of the delay line, (2) control the channel selection of a 2-channel analog multiplexer designed to switch between orthogonal photodetectors for every two axial scans, and (3) generate step functions for the x-galvanometer for every fourth axial scan. The control signal and timing diagram is illustrated in Fig. 2.
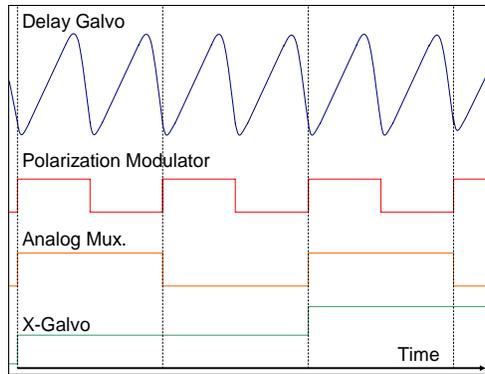
Fig. 2. Synchronized signals used to control the RSOD delay galvanometer (blue), the polarization modulator (red), the analog two-channel multiplexer (orange), and the x-galvanometer (green). Fringe data was collected during the rising slope of the pseudo-saw-tooth delay waveform (blue).

2.3 Data acquisition

Before data acquisition, the polarization modulator was tuned to produce two orthogonal linear polarization states incident on the sample. The modulator was calibrated by placing a bulk linear polarizer in the sample arm beam delivery system. A retro-reflecting mirror was used in place of a biological sample to assist in the procedure. The power returning from the mirror was measured before placing the linear polarizer into the setup. The voltages applied to the electrodes of the polarization modulator were tuned until the power returning from the sample arm retro-reflector was approximately equivalent to the initial power measurement taken without the linear polarizer present, which signified optimal alignment of the incident polarization with the linear polarizer. A polarization controller (P1) was also used to assist in this process in order to minimize the voltage sweep needed to find the first polarization state. The polarizer was then rotated 90° and the procedure was repeated to produce a linear polarization state orthogonal to the original incident state (without changing P1). The electrode voltages for the polarization modulator were recorded for each setting and were used to toggle the modulator between the two orthogonal linear polarizations states on every axial scan of the delay line.

After calibrating the polarization states of the incident sample arm beam, various muscle specimens were placed into the sample arm for imaging (data acquisition). Each muscle specimen was placed in the sample arm with the direction of the muscle fibers aligned at approximately 45° with respect to the orientation of the two orthogonal, linearly polarized, incident beams. It is well-established that anisotropic thick filaments present in skeletal muscle create a fast and slow optical axis, parallel and perpendicular to the orientation of the muscle fibers. Therefore, probing with two linearly orthogonal beams at ± 45° off axis with respect to the orientation of the muscle fibers would produce the most evident phase retardation due to sample birefringence. If either incident state were aligned with the fast or slow axis, then no birefringence would be observed. To ensure that optimal birefringence occurred with orthogonal states aligned at ± 45° with respect to the orientation of the muscle fibers, each sample was rotated ± 30° at each image location and re-imaged.

2.4 Image processing and data quantification

The output of one detector was recorded during each axial scan. Due to the phase instability introduced by the mechanical galvanometer-scanning RSOD, no useful phase information could be recovered between the orthogonal detectors. Thus, only amplitude information was extracted from the demodulated fringe data. This demodulation was implemented in software by shifting the signal spectrum to baseband and then taking the Hilbert transform, resulting in the complex analytic signal of the fringe data. The amplitude detected in the horizontal and

vertical photodetectors, A_h and A_v, respectively, was subsequently recovered by taking the magnitude of the analytic signal [16,17]. Assuming the sample has uniform optical properties (as suggested by previous PS-OCT studies on skeletal muscle tissue [16]), any birefringence in the sample will cause a sinusoidal modulation of these amplitudes, with an average spatial period of $z = \pi/k_o\delta$, where $\delta = (n_s - n_f)$, the difference in index of refraction between the slow and fast axes [18]. This is extracted from the measured data by calculating the distance between zero-crossings of $A_h - A_v$. This intensity-based quantification is not as advanced as recently-developed phase-resolved techniques [17]. However, we believe it provides sufficient information to quantify our findings and validate the hypothesis of this paper.

Structural images were generated using $10\log|A_v+A_h|$. PS-OCT birefringence images were plotted using the $\mathrm{sgn}(A_v\text{-}A_h)10\log|A_v\text{-}A_h|$ of the data. The regions of the B-scan used to calculate zero-crossing distances and subsequently the birefringence of the muscle tissue were outlined by a black box overlaid on the birefringence images (see, for example, Fig. 3(B)). These regions typically consisted of 100 A-scans, and averages were obtained from 10 A-scans in each of 10 non-overlapping segments. This analysis was performed on four separate B-scans (not shown) per mouse for both incident polarization states. For the special case of the exercised *mdx* muscle, the measured birefringence was very low ($\delta \approx 1.44 \times 10^{-3}$), making it difficult to resolve zero-crossing points; for this reason 10 A-scans from between 3 and 9 non-overlapping segments of the B-scan were averaged.. Only 3 B-scans had any measurable birefringence in this case, so it is likely that the actual birefringence of the exercised *mdx* muscle was even lower than the value reported in this study. For each specimen, black points plotted on the images mark the zero-crossings identified by our algorithm, and the mean and standard deviation was calculated for comparisons between groups. Since the tissue was probed with two orthogonal polarization states, the measured birefringence should be the same regardless of incident polarization state provided that the incident state is not perfectly aligned with the fast or slow axis. This possibility was accounted for by rotating the sample until the highest polarimetric SNR was observed [19].

2.5 Tissue processing and validation

After imaging, the muscle was dissected and flash-frozen in liquid nitrogen-cooled isopentane (Sigma) and stored at -80^oC until sectioned. The corresponding gastrocnemius muscle from the contralateral leg was dissected and drop-fixed for transmission electron microscopy (TEM). The gastrocnemius muscles samples for TEM were fixed in 2% glutaraldehyde and 2.5% paraformaldehyde in 0.2 M Sorenson's phosphate buffer, embedded in Epon 812 (Ted Pella, Inc.), sectioned at 0.1 µm using an ultramicrotome (Reichert Ultracut E), stained with uranyl acetate and lead citrate, and viewed with a transmission electron microscope (Philips CM200) at 5000x magnification. The TEM results were used to validate the arrangement and order of individual sarcomeres for the wild-type and *mdx* muscle specimens both before and after exercise. In addition, serial sections (10 µm thick) from each muscle were collected and viewed for Evans blue uptake and hematoxylin and eosin (H&E) staining in order to assess myofiber damage. Frozen sections were obtained from the distal gastrocnemius (10 sections/specimen) and observed using fluorescence and brightfield microscopy for the Evans blue and H&E sections, respectively. Muscle fiber injury was assessed by microscopic observation, by positive-fiber counting with intact membranes exhibiting Evans blue fluorescence localized to regions surrounding the fibers, and by positive-fiber counting of damaged fibers containing Evans blue fluorescence within individual fibers.

3. Results and discussion

Representative structural OCT images, PS-OCT birefringence images, and corresponding Evans blue, H&E, and TEM histology are shown in Figs. 3-6 for each specimen type. Comparing the structural OCT and PS-OCT images from the non-exercised wild-type muscle (Fig. 3(A),(B)) and the non-exercised *mdx* muscle (Fig. 4(A),(B)), little qualitative differences are noted. This is consistent with empirical observations of similarities in muscle appearance

and physical integrity during handling. The slight residual banding evident in the structural images was a result of the detectors not being perfectly balanced on consecutive axial scans. Quantitatively, the non-exercised wild-type muscle exhibited a birefringence of $\delta = (1.90 \pm 0.06) \times 10^{-3}$, and the non-exercised *mdx* murine skeletal muscle exhibited a similar level of birefringence of $\delta = (1.98 \pm 0.15) \times 10^{-3}$. These values are comparable with a previous study of the birefringence of rodent skeletal muscle ($\delta = 1.4 \times 10^{-3}$) [16]. The Evans blue images (Figs. 3(C) and 4(C)) showed a slight increase in baseline muscle injury for the *mdx* muscle. For the non-exercised *mdx* muscle, 157 Evans blue-positive fibers were counted in a total of 50 microscope fields, compared to 0 Evans blue-positive fibers in a total of 50 microscopic fields, for the non-exercised wild-type muscle. The H&E-stained histological sections (Figs. 3(D) and 4(D)) showed little structural differences when comparing wild-type and *mdx* non-exercised muscle, as expected. TEM images (Figs 3(E) and 4(E)) revealed minor ultrastructural changes in the *mdx* muscle at the level of individual sarcomeres. Note that the Evans blue and H&E-stained histological sections from *mdx* mice were viewed at 10x magnification, rather than 20x for the wild-type specimens, to visualize a greater area of the Evans blue-positive fibers.
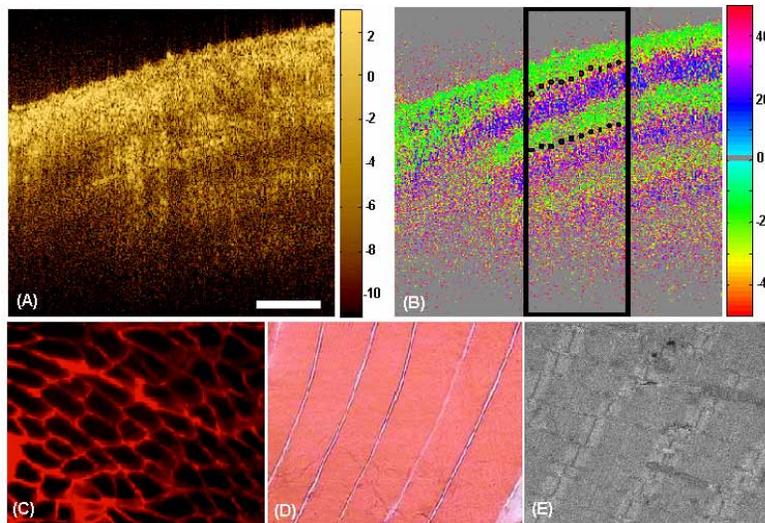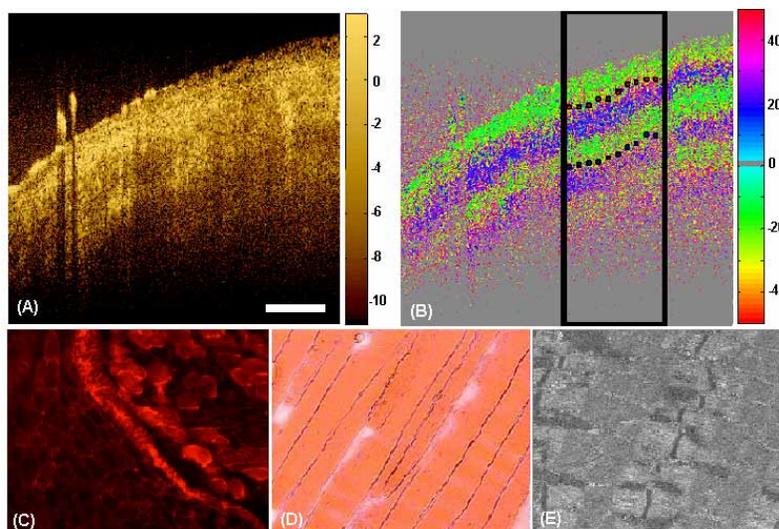

Fig. 3. Non-exercised wild-type murine skeletal muscle. A) Structural OCT image. B) False-color birefringence image. The black box outlines the region over which the mean zero-crossing distance was calculated and the black points represent the zero-crossing points identified by the algorithm. Histological images are shown using (C) Evans blue fluorescence at 20x, (D) H&E at 20x, and (E) TEM at 5000x magnifications. Scale bar represents 500 µm.

A similar imaging experiment was conducted on wild-type and *mdx* muscle in animals that were subjected to treadmill exercise prior to imaging. The PS-OCT results of skeletal muscle following exercise revealed that the wild-type muscle (Fig. 5(B)) remained highly birefringent at $\delta = (1.94 \pm 0.17) \times 10^{-3}$, similar to the images and the quantified birefringence from the non-exercised wild-type muscle (Fig. 3(B)). The validation histology (Figs. 5(C),(D),(E)) confirmed minimal changes in these wild-type muscles, with only 4 Evans blue-positive fibers in the exercised wild-type muscle (compared to 0 for non-exercised wild-type), and no significant changes on H&E sections or TEM.

The exercised *mdx* muscle (Fig. 6), however, exhibited very little birefringence at $\delta = (1.44 \pm 0.12) \times 10^{-3}$. This lack of phase retardation signified a drastic reduction in birefringence compared to the non-exercised *mdx* muscle (Fig. 4). The histological observations validate these findings. The Evans blue fluorescence (Fig. 6(C)) was strongly indicative of muscle injury. In a total of 50 fields each, there were 391 positive fibers,

compared to 157 positive fibers in the non-exercised *mdx* muscle. The H&E-stained sections (Fig. 6(D)) did not reveal significant structural changes. The TEM observations supported these findings of ultrastructural damage, and a representative TEM image (Fig. 6(E)) shows damaged sarcomeres. These results suggests that the muscle fiber structure in the *mdx* mouse was considerably more damaged during exercise, resulting in a deterioration of A-band structure and an overall loss of birefringence as detected by PS-OCT. These *mdx* mice were physically unable to complete the full duration and intensity of the exercise protocol, which the wild-type mice did complete. The PS-OCT and histological findings validate that severe ultrastructural damage was present following the portion of the exercise protocol that was completed, and that additional exercise would only induce further injury and further reduce the detected level of birefringence.

Fig. 4. Non-exercised *mdx* murine skeletal muscle. A) Structural OCT image. B) False-color birefringence image. The black box outlines the region over which the mean zero-crossing distance was calculated and the black points represent the zero-crossing points identified by the algorithm. Histological images are shown using (C) Evans blue fluorescence at 10x, (D) H&E at 10x, and (E) TEM at 5000x magnifications. Scale bar represents 500 μm.

A direct comparison of the quantified average birefringence for each of the two incident polarization states on the skeletal muscle specimens from these four groups is shown in Fig. 7. The numerical data in Fig. 7 for all the muscle types confirm the image-based qualitative observations and quantifies the amount of birefringence associated with the ultrastructure within the muscle. Similarly, Fig. 8 shows the relationship between the PS-OCT measured birefringence and the number of Evans blue-positive muscle fibers (which correlate with muscle injury). There are distinct differences between the wild-type muscle (both non-exercised and exercised) and the *mdx* muscle. The exercised *mdx* muscle clearly shows significant differences in both the measured birefringence and the number of Evans blue-positive muscle fibers, validating the findings of PS-OCT.

4. Conclusion

Polarization-sensitive OCT provides a sensitive, non- or minimally-invasive means for assessing *in vivo* changes in the birefringent properties of tissue. In this tissue optics study, the effect of varying skeletal muscle ultrastructure on the detected PS-OCT signal, and the quantified birefringence, was investigated. We found that non-exercised *mdx* murine skeletal muscle exhibited similar birefringence as non-exercised wild-type muscle. Exercising the dystrophic *mdx* muscle, however, drastically reduced the birefringence, compared to exercised wild-type muscle. The results from PS-OCT and birefringence calculations were validated

with H&E histology, Evans blue fluorescence, and TEM images, confirming the exercise-induced damage to the arrangement of individual sarcomeres present in the dystrophic *mdx* muscle.
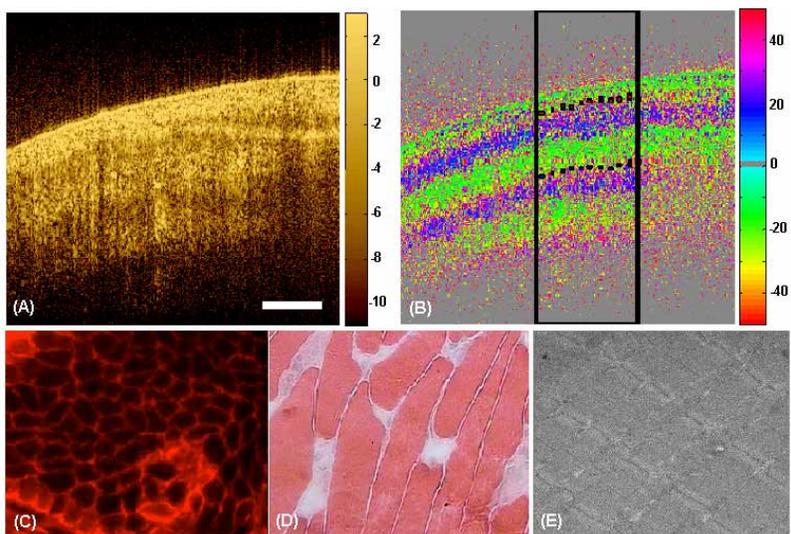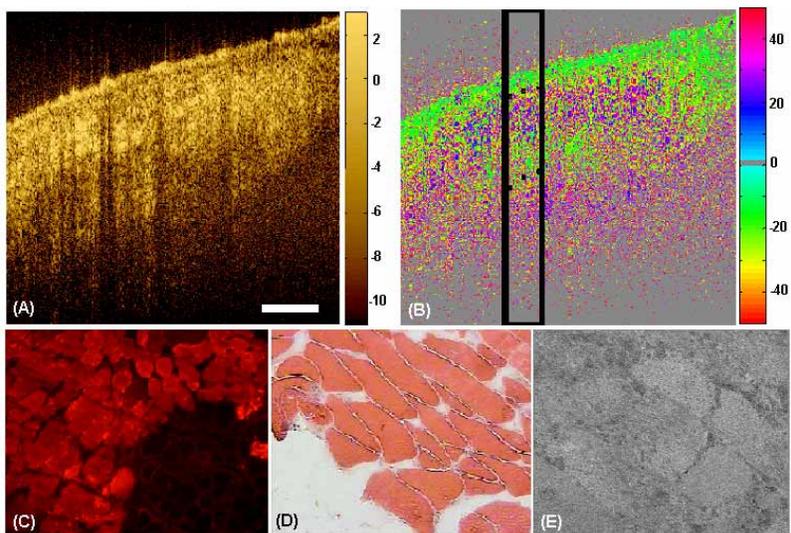

Fig. 5. Exercised wild-type murine skeletal muscle. A) Structural OCT image. B) False-color birefringence image. The black box outlines the region over which the mean zero-crossing distance was calculated and the black points represent the zero-crossing points identified by the algorithm. Histological images are shown using (C) Evans blue fluorescence at 20x, (D) H&E at 20x, and (E) TEM at 5000x magnifications. Scale bar represents 500 μm.

Fig. 6. Exercised *mdx* murine skeletal muscle. A) Structural OCT image. B) False-color birefringence image. The black box outlines the region over which the mean zero-crossing distance was calculated and the black points represent the zero-crossing points identified by the algorithm. Histological images are shown using (C) Evans blue fluorescence at 10x, (D) H&E at 10x, and (E) TEM at 5000x magnifications. Scale bar represents 500 μm.
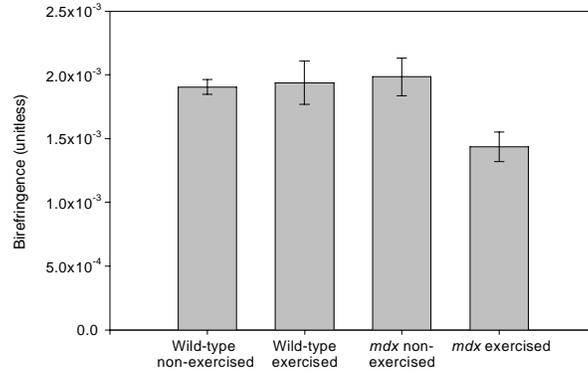
Fig. 7. Quantitative comparison of birefringence values from skeletal muscle types. Error bars represent the standard deviation of the birefringence.
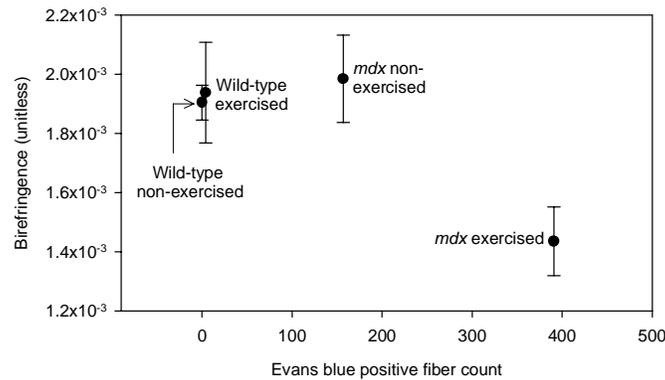

Fig. 8. Plot showing calculated birefringence values vs. measured Evans blue positive fiber count for the four muscle types. Error bars represent standard deviation of the birefringence.

These results suggest that PS-OCT can detect birefringence changes due to the ultrastructural alterations occurring in the sarcomeres of skeletal muscle due to genetic alterations and due to damage during exercise. This damage can be attributed to the lack of dystrophin in the *mdx* muscle, and hence, the lack of preservation of structural integrity following exercise. The preservation of phase retardation after exercise in the wild-type muscle further supports that ultrastructural order (A-band organization) was maintained due to the abundance of these structural proteins.

Future studies will include the implementation of quantitative phase-based PS-OCT measurements following hardware upgrades to enable more phase-stable imaging methods. Larger numbers of specimens will be imaged to determine levels of statistical differences of birefringence measurements within single specimens, between specimens within a group, and between different groups. Based on the qualitative and quantitative findings presented in this paper, we demonstrate that a direct relationship exists between the ultrastructure of skeletal muscle fibers and the PS-OCT-detected birefringence.

Acknowledgments